Visualization of ultrafast melting initiated from radiation-driven defects in solids

Mianzhen Mo, Samuel T. Murphy, Zhijiang Chen, Paul C. M. Fossati, Renkai Li, Yongqiang Wang, Xijie Wang, Siegfried Glenzer

MATERIALS SCIENCE

Visualization of ultrafast melting initiated from radiation-driven defects in solids

Mianzhen Mo[1]*, Samuel Murphy[2]*, Zhijiang Chen[1], Paul Fossati[3,4], Renkai Li[1], Yongqiang Wang[5], Xijie Wang[1], Siegfried Glenzer[1]*

Materials exposed to extreme radiation environments such as fusion reactors or deep spaces accumulate substantial defect populations that alter their properties and subsequently the melting behavior. The quantitative characterization requires visualization with femtosecond temporal resolution on the atomic-scale length through measurements of the pair correlation function. Here, we demonstrate experimentally that electron diffraction at relativistic energies opens a new approach for studies of melting kinetics. Our measurements in radiation-damaged tungsten show that the tungsten target subjected to 10 displacements per atom of damage undergoes a melting transition below the melting temperature. Two-temperature molecular dynamics simulations reveal the crucial role of defect clusters, particularly nanovoids, in driving the ultrafast melting process observed on the time scale of less than 10 ps. These results provide new atomic-level insights into the ultrafast melting processes of materials in extreme environments.

INTRODUCTION

Understanding the structural dynamics of ultrafast laser-induced melting is important for applications ranging from laser micromachining (*1*) to high-energy density physics experiments (*2*). According to thermodynamics, melting occurs when temperature increases drive the free energy of the liquid below that of the solid. At the melting temperature, melt fronts nucleate heterogeneously from either free surfaces or grain boundaries (*3*, *4*). Suppression of surface melting, for example, through ultrafast heating, leads to the homogeneous nucleation of liquids in the bulk of a superheated solid (*5*, *6*), indicating the importance of kinetics in phase transformations.

Theories for how homogeneous melting proceeds fall into two categories: (i) nucleation at point or extended defects (*7*, *8*) or (ii) the formation of an initial liquid nucleus aided by thermal fluctuations without preferential nucleation sites (*9*). Whether they drive melting or not, point defects are observed to proliferate as the temperature approaches the melting point. In metals, for example, the vacancy concentration reaches 0.37% at the melting temperature, followed by a rapid increase of 10% during the melting process (*10*, *11*).

Direct experimental observations of nucleation processes have previously not been possible because of the small time and length scales involved. However, recent advances in time-resolved diffraction techniques based on ultrafast electron (*12*–*14*) and x-ray pulses (*15*, *16*) enable us to study the transient atomic dynamics with femtosecond temporal resolution. In particular, the advent of x-ray free-electron lasers (XFELs) has provided extremely bright x-ray pulses for diffraction measurements and has been successfully used in studying structural dynamics of matter under extreme conditions (*16*, *17*). Time-resolved diffraction offers a direct means to determine the quantitative structural information through the atomic pair correlation function (PCF) (*12*, *18*), the construction of which, however, requires the measurement of diffraction data over a large momentum transfer range. For diffraction measurements with field-accelerated electrons, this can be readily met because of their short de Broglie wavelengths (0.34 pm for 3.2-MeV electrons), whereas for measurements with XFELs, it requires high-energy x-rays (50 pm for 25-keV x-rays) that have recently become available for experiments (*19*).

A previous demonstration of PCF using 30-keV electron pulses required averaging of a substantial number of shots (1200), thus restricting measurements to a few data points that only covered the initial solid phase and the final liquid phase (*12*). On the other hand, the performance of ultrafast electron diffraction (UED) has been greatly improved with megaelectronvolt electrons (*20*, *21*). The bunch charge is significantly enhanced because of the reduced space charge effect, enabling single-shot measurements with high signal-to-noise ratios (SNRs). Furthermore, multiple elastic scattering effects are negligible at these energies because of the relatively large elastic mean free path.

Here, we study the structural dynamics of femtosecond laser-induced melting of tungsten (W) containing radiation-induced defects. We measured time-resolved electron diffraction patterns with sufficient momentum transfer range that provides accurate PCF results. We observed that the W subjected to 10 displacements per atom (dpa) of radiation damage undergoes a melting transition within 10 ps, indicated by the loss of the long-range order associated with the crystalline phase and the appearance of the short-range order with the liquid structure. This is in contrast to the pristine W case in which incomplete melting was observed with considerable crystallinity still persisting on time scales in excess of 20 ps.

Two-temperature molecular dynamics (2T-MD) simulations were performed to understand these observations and showed that defect clusters, particularly nanovoids, play a crucial role in driving the overall melting process in the radiation-damaged W. This is attributed to the fact that the melting process initiated from the embedded nanovoids continues at temperatures below the equilibrium melting point. This unusual melting behavior is explained by the thermodynamic analysis on the stability of small crystalline clusters surrounded by undercooled liquid.

In addition, the comparison of high-quality PCF data between radiation-damaged and pristine W resolved the loss of the coordination

[1]SLAC National Accelerator Laboratory, Menlo Park, CA 94025, USA. [2]Engineering Department, Lancaster University, Lancaster LA1 4YW, UK. [3]Department of Materials, Imperial College London, South Kensington, London SW7 2AB, UK. [4]DEN—Service de la Corrosion et du Comportement des Matériaux dans leur Environnement (SCCME), CEA, Université Paris Saclay, F-91191 Gif-sur-Yvette, France. [5]Materials Science and Technology Division, Los Alamos National Laboratory, Los Alamos, NM 87545, USA.
*Corresponding author. Email: mmo09@slac.stanford.edu (M.M.); samuel.murphy@lancaster.ac.uk (S.M.); glenzer@slac.stanford.edu (S.G.)

number. On the basis of the first two nearest neighbor shells, we found a vacancy population of ~5% in the radiation-damaged W, which determines the initial condition for MD simulations. Using the measured initial conditions, a proper interatomic potential and the experimentally determined electron-phonon coupling strength in the MD simulations result in excellent agreement between measured and simulated melting kinetics.

This is the first measurement of the melting dynamics in materials with radiation-induced defects. Combining the UED experiments with MD simulations provides a complete picture of the structural evolution of ultrafast laser-induced melting of radiation-damaged W with important implications for designing new materials and predicting their long-term degradation in extreme environments (*22*–*24*).

RESULTS AND DISCUSSION

We performed UED studies on 30-nm-thick polycrystalline W films under nonreversible photoexcitation conditions. These W thin films were deposited on 50-nm-thick free-standing amorphous Si_3N_4 membranes. Radiation damage to the targets was carried out before the pump-probe experiments through 200-keV Cu^+ ion bombardment at room temperature condition (see Materials and Methods). To study the melting dynamics of different defect concentrations, we examined two displacement levels of 1 and 10 dpa and compared them with pristine targets. The high-energy Cu^+ projectiles displace lattice atoms, resulting in displacement cascades and the production of point defects (*25*, *26*). At room temperature, vacancy defects produced during the cascade are immobile. In contrast, interstitial defects are highly mobile and diffuse to surfaces or grain boundaries. Consequently, the irradiated film is expected to be populated with randomly distributed vacancy defects, some of which may form clusters.

As shown in Fig. 1, W targets were excited with 130-fs [full width at half maximum (FWHM)] and 400-nm laser pulses with flat top–like intensity profiles of ~420 μm in diameter. Time-resolved diffraction

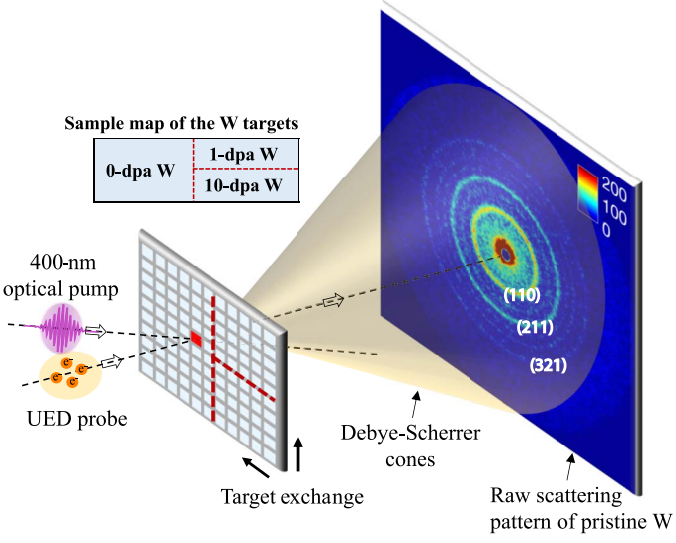

Fig. 1. Schematic of the experimental setup. The W targets were pumped by 130-fs and 400-nm laser pulses and probed by UED at megaelectronvolt energies. Radiation damage to the targets at different defect densities was prepared before the pump-probe experiments. The displayed diffraction pattern is the typical four-shot average pattern of the unpumped pristine W target.

experiments were performed at normal incidence in transmission geometry with relativistic electrons with kinetic energy of 3.2 MeV. The relativistic electrons were focused onto the targets with a diameter of ~120 μm (FWHM), bunch charges of 20 fC, and pulse durations of ~350 fs (FWHM). The scattered electrons of the targets were recorded by a phosphor-based single-electron sensitive detector located 3.2 m downstream, providing a maximum momentum transfer Q of ~10 $Å^{-1}$ and a Q resolution of ~ 0.35 $Å^{-1}$. Here, Q is defined as $Q = 4\pi \sin\theta/\lambda$, with θ and λ represent the scattering angle and the de Broglie wavelength of the electrons (λ ~ 0.34 pm for 3.2-MeV electrons), respectively. A total number of four scattering images were recorded and averaged at each time point, which provides sufficient SNR to perform the PCF analysis.

Time-resolved electron diffraction data

Figure 2 shows the temporal evolution of the diffraction signals for the pristine (Fig. 2A) and irradiated (Fig. 2, B and C) W targets. These targets were excited at the same absorbed pump fluence of 46 mJ/cm^2, which is close to but below the expected complete melting threshold of pristine W (52 mJ/cm^2) (see Materials and Methods). The time-resolved scattering pattern shows three distinctive characteristics: (i) the decay of Laue diffraction peaks (LDPs) intensity due to the Debye-Waller effect, followed by structural phase changes, as indicated by the disappearance of (211) (Fig. 2C); (ii) the increase of the thermal diffuse scattering (TDS) signal over the measured Q range, which is visible in regions between diffraction peaks; and (iii) the rise of the highly disordered liquid scattering signal, the first peak of which overlaps with the LDP (110). This feature broadens within the first 5 ps. At a given time delay, the magnitude of the LDP decay increases with the defect population. This is evident from Fig. 2 (D to F) that compares the raw diffraction images measured at 20 ps. The diffraction peak signals in 10-dpa W are no longer observable at 20 ps, suggesting the formation of a fully liquid state. In addition, the sample exhibits an enhancement in the TDS background and an increased broadening of the first liquid peak. Figure 2 (G to I) shows the temporal evolution of the (211) intensity, the TDS signal at 8.0 ± 0.05 $Å^{-1}$, and the liquid scattering signal at 2.2 ± 0.05 $Å^{-1}$. To understand the dynamics of these signals, we performed monoexponential fits to the data (*13*), and the resulting 1/*e* time constants are provided in Fig. 2 (G to I). The increase of TDS signal shows the fastest dynamics, followed by the LDP decay, and the liquid dynamics is the slowest. This nonsynchronous behavior is observed with both the pristine and the irradiated targets and is characteristic of a thermal heating process. Note that the observed similar time constants of both (211) and TDS dynamics between the pristine and irradiated targets indicate a similar lattice heating process in these three samples despite their different melting behaviors.

Time-resolved PCF

The ultrafast structural changes in W can be further illustrated by analyzing the temporal evolution of the real-space correlation functions (see the Supplementary Materials for additional details). In particular, the correlations in atomic positions can be expressed in the form of the average PCF $H(r)$ calculated through a sine Fourier transform of the diffracted intensity (*12*, *18*). Figure 3 compares $H(r)$ for the pristine and 10-dpa samples at −2, 2, 4, and 20 ps. We also computed the $H(r)$ directly from the atomic configurations obtained from 2T-MD simulations (*27*). Radiation damage due to irradiation to 10 dpa was represented by introducing a vacancy concentration of 5% at random locations into the simulation supercell and by annealing for 0.5 ns at

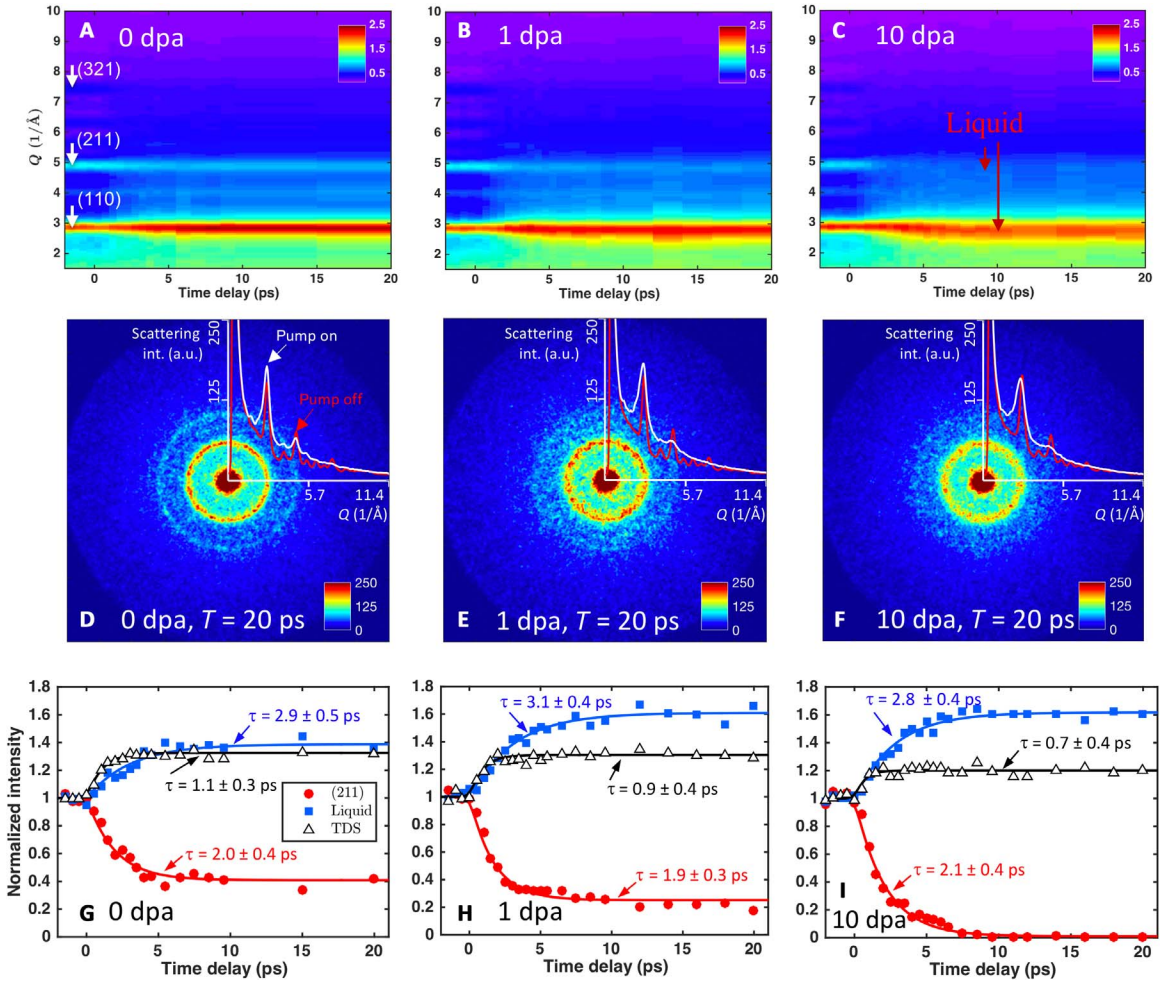

Fig. 2. Temporal evolution of the measured megaelectronvolt electron diffraction signal at absorbed pump fluence of 46 mJ/cm^2. (**A** to **C**) Scattering intensities as a function of *Q* and *T* for 0-, 1-, and 10-dpa W samples. (**D** to **F**) Raw diffraction images taken at *T* = 20 ps for the three types of samples. Radially averaged lineouts (white solid lines) and their reference lineouts (red solid lines) of pump-off diffraction images are overlaid on the top-right quadrants. a.u., arbitrary units. (**G** to **I**) Time traces of the decay of (211) peak (red dots), the rise of the liquid scattering signal at 2.2 ± 0.05 Å^{-1} (blue squares), and the rise of TDS at 8.0 ± 0.05 Å^{-1} (black empty triangles) for the three types of W. Normalization of the data was done relative to the scattering intensity averaged over all negative delay points. Solid lines represent fits to the data with convolutions of single exponentials and a Gaussian function for the system response. The 1/*e* time constants of the fits, denoted by τ, are given in (G) to (I).

300 K. The 5% value was chosen to match the reduction of the coordination number of the first two nearest neighbor shells observed from the experiments of nonheated samples (*11*).

Before laser excitation (−2 ps), *H*(*r*) exhibits long-range correlations as expected in a crystalline material. In principle, each peak in *H*(*r*) corresponds to a specific interatomic distance between a pair of atoms in the body-centered cubic (bcc) structure of W (Fig. 3E). The broadening and overlapping of atomic peaks are observed in the experimental data due to the limited *Q* range of the scattered intensity (Fig. 3A). For instance, the first peak at *r* = 2.85 ± 0.05 Å consists of the first (*r* = 2.73 Å) and second (*r* = 3.16 Å) nearest neighbor shells of a bcc W lattice. This is confirmed by the coordination number of this peak, which is calculated to be 14 ± 0.3 for the pristine W that is equal to the sum of 8 and 6 for the first two nearest neighbor shells of bcc W, visible as two distinct peaks in the 2T-MD simulation results. Another interesting feature of both experimental and simulated *H*(*r*) at negative delay is the noticeable reduction in peak amplitudes of all observed atomic peaks in the 10-dpa sample, implying that decreases in coordination number are associated with the displacement damage from the high-energy ion bombardment. We calculated the coordination number loss for the first measured peak to be 0.6 ± 0.3, which is matched with MD simulations.

The temporal evolution of *H*(*r*) following laser excitation is illustrated in Fig. 3 (B to D and F to H) for experiments and simulations, respectively. In the pristine W case, the UED data show a clear decrease of peak intensities as the lattice temperature increases in the first 4 ps, after which time the changes are considerably slowed down, especially in the small *r* region. Despite the intensity reduction, the peaks remain well defined after 20 ps, confirming the presence of long-range crystalline ordering. In contrast, the changes of *H*(*r*) in 10-dpa W show a substantial peak height reduction, and noticeable broadening and merging of peaks. At 4 ps, the correlation peaks at *r* > 6-Å region diminish. These observations imply a substantial loss of the long-range order. At 20 ps, the remaining peaks continued to broaden and decline in intensity,

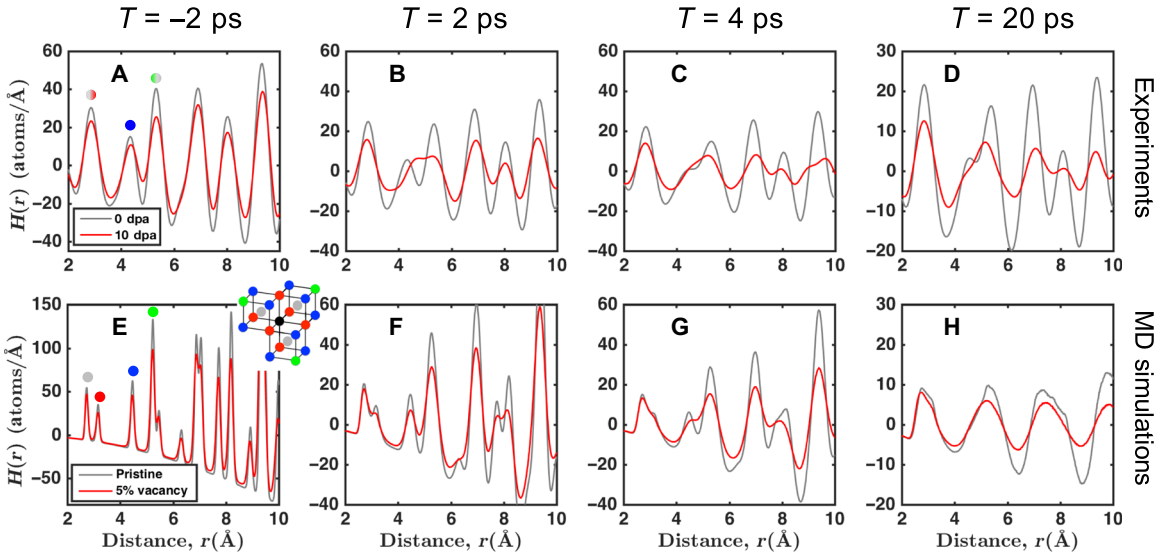

Fig. 3. Snapshots of the time-dependent PCF *H*(*r*). (**A** to **D**) Experimental *H*(*r*) inferred at selective time delays for 0- (gray curves) and 10-dpa (red curves) W targets. (**E** to **H**) MD simulated *H*(*r*) at the same time delays for perfect W (gray curves) and defective W with 5% of vacancies embedded (red curves). The interatomic spacings for bcc W lattice are shown in the inset for the first four atomic peaks. Atoms of given radial distance from the central black atom are displayed in the same color. Observed atomic peaks of the same radial distances are labeled with the same solid circles on *H*(*r*) curves that are shown in (A) and (E). Merging of adjacent atomic peaks, indicated by solid circles of mixing colors in (A), is seen with the experimental *H*(*r*) due to the limited *Q* range of the measured scattering signal.

suggesting progressive changes to the short- or medium-range correlations in atomic positions as the system transitioned to a complete liquid.

The simulated correlation peaks show noticeable broadening and reduction of their peak heights during the solid-liquid phase transition. Merging of adjacent peaks is found to occur at similar regions as observed in the experiments, for example, the region between $r = 4$ Å and $r = 6$ Å. At 20 ps, the long-range order is completely lost in the 5% vacancy W, and what remained are the short-range correlations that correspond to a highly disordered state. On the other hand, the pristine case still shows the existence of long-range correlations at this time, indicated by the deviation from the ideal sinusoidal behavior (Fig. 3H).

Note that the interatomic potential plays a central role in determining the material behaviors and properties in MD simulations. Our measured time-resolved diffraction data hence provide an important dataset for assessing the applicabilities of the available interatomic potential models for W. The overall agreement with the experimental results in predicting the temporal evolution of *H*(*r*) favors the extended Finnis-Sinclair potential for W (*28*) adopted in our MD simulations.

MD simulations of ultrafast melting

To understand the physics behind the experimental observations of different melting behaviors between the pristine and irradiated W targets, we examine the atomic trajectories from 2T-MD simulations performed with the DL_POLY code (see Materials and Methods) (*29*). Figure 4 shows snapshots of the atomic configurations and demonstrates the role of radiation-induced defects on melting. Both pristine and irradiated samples experience similar increases in the lattice temperature (Fig. 4K), in good agreement with the experimental observations (Fig. 2, G to I). For the pristine sample, the temperature increase results in the appearance of undercoordinated atoms evenly distributed throughout an otherwise crystalline film (Fig. 4E). In contrast, the irradiated sample undergoes the solid-liquid transformation within 20 ps. This is illustrated in Fig. 4 (F to J), where the concentration of undercoordinated and amorphous atoms increases such that there are only small pockets of crystalline material present after 20 ps. Of particular interest are the nanoscale features present due to defect clustering and nucleation. Figure 4 (L to O) shows the undercoordinated atoms surrounding one big nanovoid at selective time delays. As energy is deposited into the lattice, these undercoordinated atoms move into empty space provided by the void and their coordination decrease markedly as they find themselves with amorphous local environments. Amorphization of this nanovoid occurs within 5 ps, a long time before the local temperature reaches the melting temperature ($T_m = 3695$ K). This amorphous cluster then acts as a nucleation center, promoting the overall melting of the film.

After amorphization of nanovoids, the melting process continues below the melting temperature in the irradiated sample. This can be understood based on the classical nucleation theory that considers the Gibbs free energy change, $\Delta G(r)$, upon the formation of a spherical solid nucleus of radius r in an undercooled liquid (*9*, *30*)

$$\Delta G(r) = -\frac{4}{3}\pi r^3 \Delta G_v + 4\pi r^2 \gamma_{sl} \quad (1)$$

where ΔG_v is the difference in volumetric free energy density between the solid and liquid and γ_{sl} is the interfacial tension at the liquid-solid interface. For small undercoolings, $\Delta T = T_m - T$, ΔG_v can be approximated by $\Delta H_m \Delta T / T_m$, with ΔH_m being the latent heat expressed in units of energy per volume. For a given ΔT, the critical nucleus size $r^* = 2\gamma_{sl} T_m / (\Delta H_m \Delta T)$ can be obtained from Eq. 1, which corresponds to the barrier height of ΔG and determines the length scale beyond which growth of the cluster becomes favorable. For a solid cluster with a radius of r, the expression of r^* can be formulated to give the critical undercooling temperature, T^* (*30*)

$$T^* = T_m \left[1 - \frac{2\gamma_{sl}}{\Delta H_m} \frac{1}{r}\right] \quad (2)$$

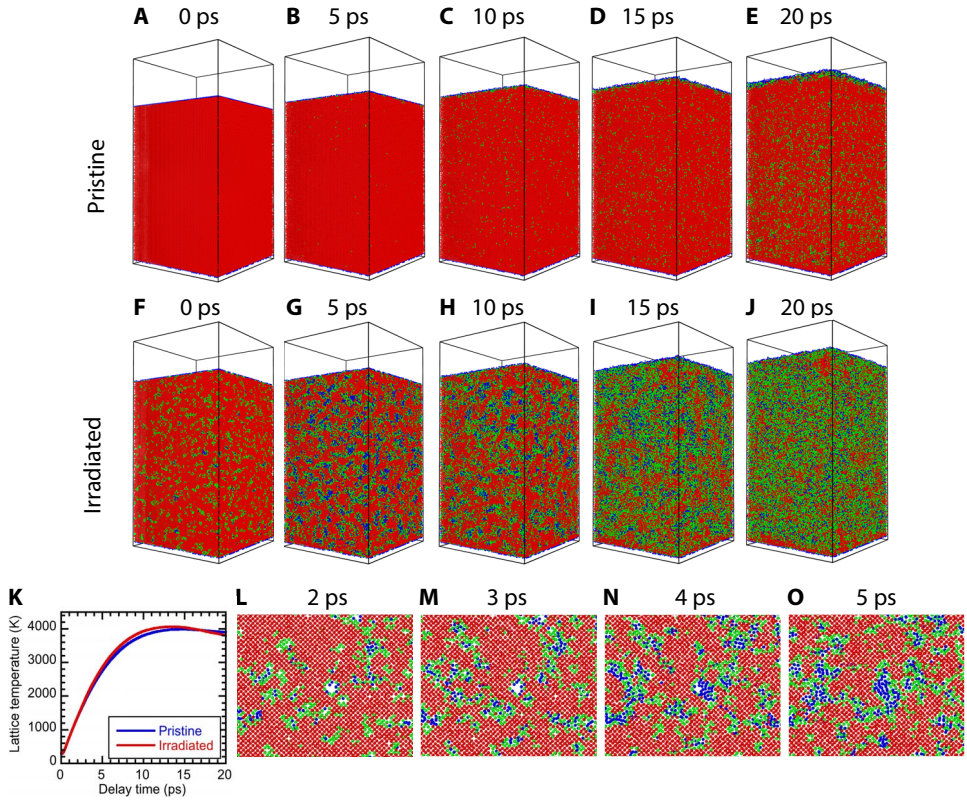

Fig. 4. 2T-MD simulated ultrafast laser-induced melting of 30-nm-thick W. The melting is driven by 130-fs and 400-nm lasers at absorbed pump fluence of 46 mJ/cm^2. (**A** to **E**) Snapshots of atomic configurations for pristine W thin film. (**F** to **J**) Same as in (A) to (E) but for irradiated thin film with 5% of vacancy defects. Atoms are colored according to their connectivity, where red spheres have a connectivity of 13 to 14 and represent crystalline atoms, green spheres have connectivity of 11 to 12 and represent strongly undercoordinated, and blue spheres have a connectivity of less than 11 and represent atoms in an amorphous/disordered state. (**K**) Graph showing the temporal evolution of the lattice temperature for the pristine and irradiated samples following laser excitation. (**L** to **O**) Close-ups of the irradiated sample that illustrate the melting nucleation surrounding one big nanovoid.

which corresponds to the equilibrium between the solid cluster and the surrounding liquid. At the condition when $T > T^*$, the dissolution of the solid cluster leads to the decrease of Gibbs free energy and thereby is favorable. Equation 2 indicates that T^* will drop by decreasing the size of the solid cluster. Using the following parameters for W, $\Delta H_m = 5.4 \times 10^9$ J/m^3 (*31*) and $\gamma_{sl} = 0.59$ J/m^2 (*32*), Eq. 2 predicts $T^* = 2888$ K for a solid cluster with $r = 1$ nm, which is only 78% of the melting temperature for W. This explains what we observed from the MD simulations of the irradiated samples. The initial amorphization process of the nanovoids in the early heating stage further separates the irradiated solid into many small nanocrystallites that are surrounded by liquid regions. This, in turn, suppresses the melting temperature of those nanocrystallites according to Eq. 2 and leads to the observed rapid melting in irradiated W.

CONCLUSIONS

Our UED measurements investigated the ultrafast solid-liquid phase transition in W highly populated with defects. The experiments provide highly detailed structural information and subpicosecond time resolution, enabling direct testing of atomistic simulations. The observation of rapid melting for irradiated W is understood with 2T-MD simulations, illustrating the driven nature of nucleation seeds from the embedded defect clusters. Further MD simulations at a much slower heating rate show that the embedded defects may anneal rather than favor nucleation, suggesting the importance of heating rate in rendering the observed rapid melting in irradiated W. Our time-resolved electron diffraction results combined with MD simulations provide a complete atomic-level picture of the ultrafast melting mechanism in systems highly populated with defects. These results have tested MD simulations for the understanding of the long-term degradation of materials under extreme environments.

MATERIALS AND METHODS

Experimental details

The pump-probe experiments were performed in the Accelerator Structure Test Area facility at SLAC National Accelerator Laboratory (*33*, *34*). The megaelectronvolt electrons for diffraction studies were achieved by a Linac Coherent Light Source (LCLS)–type photocathode radio frequency (rf) gun. The rf gun was powered by a pulse-forming network–based modulator and a 50-MW S-band klystron. The relativistic electrons were focused by two separated solenoids installed after the rf gun onto the target. The electron detector was located 3.2 m away from the sample and consisted of a P43 phosphor screen, a lens system, and a sensitive electron-multiplying charge-coupled device (CCD) (EMCCD) camera (Andor iXon Ultra 888). In the middle of the phosphor screen, there was a 1.6-mm-diameter through-hole to prevent the

zero-order diffraction signal from saturating the CCD image at high gain during the experiments.

The pristine targets were 30-nm-thick polycrystalline W grown on 50-nm-thick amorphous Si_3N_4 membranes (350 × 350 μm) supported by a 2″ by 1″ Si wafer [manufactured by Norcada (*35*)]. The scattering signal of a 50-nm-thick amorphous Si_3N_4 membrane was measured to be much weaker than that of 30-nm-thick W (see the Supplementary Materials for additional details). The targets at different areas of the same Si wafer were irradiated at different fluences of high-energy Cu^+ ions to obtain different defect densities. The pristine and predamaged targets were excited by 130-fs and 400-nm laser pulses at 4° incidence angles with flat top–like intensity profiles. The flat-top pump profile was achieved with 10:1 imaging of an aperture outside the target chamber by a single lens with a focal length of 25 cm. The root mean square intensity variation is less than 5% of the averaged value within the full probed area, ensuring uniform excitation of the sample. The absorption coefficients of 400-nm laser light for the unirradiated and irradiated W thin films were measured to be the same in an offline reflection and transmission experiment.

Ion irradiation

High-energy ion irradiation on the W targets was carried out at room temperature using the 200-kV Danfysik Research Ion Implanter at the Ion Beam Materials Laboratory in Los Alamos National Laboratory. Two different damage doses of 1 and 10 dpa were obtained using implantation fluences of 2.88×10^{14} and 2.88×10^{15} ions/cm^2 under an ion flux of approximately 2×10^{12} ions/cm^2 s^{-1}. The ion fluence to damage dose conversion was done by using the SRIM (Stopping and Range of Ions in Matter) 2013 Monte Carlo code (*36*) with the full cascade mode using the threshold W displacement energy of 90 eV (*37*). The displacement levels quoted here do not represent the final damage to W since thermal effects are not considered in the SRIM calculations, which, however, does not affect our study reported here. For convenience, we refer the two irradiated targets to as 1 and 10-dpa W in the main text.

Complete melting threshold

The complete melting threshold is the energy that would be sufficient to completely melt the film. This complete melting threshold can be expressed in terms of absorbed pump fluence, F_m, and is given by (*30*)

$$F_m = \left(\int_{300}^{T_m} C_l(T)dT + \int_{300}^{T_m} C_e(T)dT + \Delta H_m \right) L \quad (3)$$

where L is the thin film thickness, T_m is the nominal melting temperature, and ΔH_m is the latent heat. Equation 3 implies that the complete melting threshold is the amount of energy that is required to heat the material from room temperature to its equilibrium melting temperature and to melt the entire film at the melting temperature. Using the following parameters: ΔH_m = 280 kJ/kg (*31*), T_m = 3695 K (*31*), and taking into account the temperature dependence of $C_l(T)$ (*38*) and $C_e(T)$ (*39*), we estimated F_m to be approximately 52 mJ/cm^2 for 30-nm-thick W film.

2T-MD simulation details

The two temperature models used here were developed by Duffy and Rutherford and implemented in the DL_POLY code (*29*, *40*). The crystal was represented using a classical MD supercell. This supercell was coupled to a continuum cell representing the electronic subsystem with energy able to transfer between the two to mimic electron phonon coupling. The electronic subsystem was represented using the following heat diffusion equation

$$C_e(T_e)\frac{\partial T_e}{\partial t} = \nabla \cdot (\kappa_e \nabla T_e) - G_{ei}(T_e - T_i) + S(z,t) \quad (4)$$

where κ_e is the electronic heat conductivity and $S(z, t)$ is a source term that represents the energy deposited by the laser. The laser pulse is assumed to be Gaussian in time, with an exponentially decreasing amplitude as a function of depth in the film, z, that is

$$S(z,t) = \left(\frac{2F}{l_p t_p} \frac{\sqrt{\ln 2}}{\pi} \right) e^{-4\ln 2 (t-t_0)^2 / t_p^2} e^{-z/l_p} \quad (5)$$

where F is the fluence from the experiments (46 mJ/cm^2), l_p is the optical penetration depth of the sample at the wavelength of the pulse length (12.5 nm), t_p is the duration of the pulse (130 fs), and t_0 is the time zero corresponding to the maximum of the laser pulse on the sample surface. For thin films, κ_e can be considered infinite and so the first term on the right-hand side of Eq. 4 disappears.

The traditional equations of motion governing the evolution of atoms in the MD supercell are modified, such that

$$m_i \frac{\partial \mathbf{v}_i}{\partial t} = \mathbf{F}_i - \gamma \mathbf{v}_i + \mathbf{f}_L(T_e) \quad (6)$$

where v_i is the velocity of an atom with mass, m_i. $\mathbf{F}_i$ is the classical force acting on the atom calculated using an extended Finnis-Sinlair model (*28*), γ represents a frictional drag force, and $\mathbf{f}_L$ is the stochastic force. The extended Finnis-Sinclair potential was selected as it accurately reproduces the melting temperature of W. The friction and stochastic terms allow energy to be added or removed from the ions to represent energy transfer with electrons; hence, γ is related to the electron-phonon coupling strength according to

$$\gamma = \left(\frac{V}{N'} \right) \frac{m}{3k_B} G_{ei} \quad (7)$$

where V is the volume of a coarse grain ionic voxel, N' is the number of atoms in the voxel, and G_{ei} is the electron-phonon coupling strength. In our 2T-MD simulations, we set G_{ei} as a constant of 2.0×10^{17} W/m^3 K^{-1}, which was inferred from the Debye-Waller factor measurements performed at below the damage threshold of W (see the Supplementary Materials for additional details).

To represent the experimental thin films simulation, supercells were created by taking 62 × 62 × 94 repetitions of the bcc W unit cell, resulting in a film that is 30 nm thick with a cross-sectional area of 383.85 nm^2. To represent irradiation-induced defects, a 5% concentration of vacancy defects was randomly introduced into the sample. The total number of atoms was kept approximately constant by adding layers to the top of the sample. Simulation supercells were equilibrated for 500 ps, with a 1-fs time step at 300 K under constant volume and temperature (NVT) conditions using the Nose-Hoover thermostat with a relaxation time of 0.01 ps. After equilibration, atoms in the bottom 5 Å were tethered using a harmonic potential to their initial lattice site to represent bonding to the substrate. The simulation supercells were then subjected to a 130-fs laser pulse delivering 46 mJ/cm^2.

The connectivity was calculated using the core dynamics package. Here, we define the connectivity as the number of lattice atoms within the limit of the second nearest neighbor shell, which is determined dynamically. Note that this excludes interstitial-type atoms, ensuring that the maximum connectivity is then 14 for the ideal bcc-structured materials. Neglect of the interstitial atoms in the determination of the connectivity makes identification of amorphous regions easier.

SUPPLEMENTARY MATERIALS

Supplementary material for this article is available at http://advances.sciencemag.org/cgi/content/full/5/5/eaaw0392/DC1

Supplementary Text

Fig. S1. Megaelectronvolt electron scattering intensity of unpumped samples.

Fig. S2. Lattice dynamics blow the damage threshold.

Fig. S3. The radial density function of pristine W inferred at time delay of −2 ps.

Table S1. Comparison of the measured and expected results of radial distances and coordination numbers for the first few nearest neighbor shells of bcc W lattice.

Movie S1. Temporal evolution of the megaelectronvolt-electron diffraction pattern for the pristine 30-nm-thick W as it underwent ultrafast laser-induced melting at absorbed pump fluence of 46 mJ/cm^2.

Movie S2. The same as movie S1 but for W that is subject to 1-dpa radiation damage.

Movie S3. The same as movie S1 but for W that is subject to 10-dpa radiation damage.

Movie S4. 2T-MD simulated ultrafast laser-induced melting of pristine W.

Movie S5. The same as movie S4 but for the irradiated W with 5% of vacancy defects.

Movie S6. Close-up of a selected area in movie S5 showing the melting nucleation surrounding one big nanovoid.

References (*41*–*47*)

REFERENCES AND NOTES

1. R. R. Gattass, E. Mazur, Femtosecond laser micromachining in transparent materials. *Nat. Photonics* **2**, 219–225 (2008).
2. S. H. Glenzer, R. Redmer, X-ray Thomson scattering in high energy density plasmas. *Rev. Mod. Phys.* **81**, 1625–1663 (2009).
3. J. G. Dash, History of the search for continuous melting. *Rev. Mod. Phys.* **71**, 1737–1743 (1999).
4. U. Dahmen, S. Hagège, F. Faudot, T. Radetic, E. Johnson, Observations of interface premelting at grain-boundary precipitates of Pb in Al. *Philos. Mag.* **84**, 2651–2662 (2004).
5. B. Rethfeld, K. Sokolowski-Tinten, D. von der Linde, S. I. Anisimov, Ultrafast thermal melting of laser-excited solids by homogeneous nucleation. *Phys. Rev. B* **65**, 092103 (2002).
6. D. S. Ivanov, L. V. Zhigilei, Kinetic limit of heterogeneous melting in metals. *Phys. Rev. Lett.* **98**, 195701 (2007).
7. H. J. Fecht, Defect-induced melting and solid-state amorphization. *Nature* **356**, 133–135 (1992).
8. L. Gómez, A. Dobry, C. Geuting, H. T. Diep, L. Burakovsky, Dislocation lines as the precursor of the melting of crystalline solids observed in Monte Carlo simulations. *Phys. Rev. Lett.* **90**, 095701 (2003).
9. D. A. Porter, K. E. Easterling, *Phase Transformations in Metals and Alloys* (Chapman and Hall, 1992).
10. T. Górecki, Vacancies of changes of 1st coordination sphere radius of metals at melting-point. *Z. Metallkd.* **67**, 269 (1976).
11. T. Górecki, Comments on vacancies and melting. *Scripta Met.* **11**, 1051–1053 (1977).
12. B. J. Siwick, J. R. Dwyer, R. E. Jordan, R. J. D. Miller, An atomic-level view of melting using femtosecond electron diffraction. *Science* **302**, 1382–1385 (2003).
13. R. Ernstorfer, M. Harb, C. T. Hebeisen, G. Sciaini, T. Dartigalongue, R. J. D. Miller, The formation of warm dense matter: Experimental evidence for electronic bond hardening in gold. *Science* **323**, 1033–1037 (2009).
14. M. Z. Mo, Z. Chen, R. K. Li, M. Dunning, B. B. L. Witte, J. K. Baldwin, L. B. Fletcher, J. B. Kim, A. Ng, R. Redmer, A. H. Reid, P. Shekhar, X. Z. Shen, M. Shen, K. Sokolowski-Tinten, Y. Y. Tsui, Y. Q. Wang, Q. Zheng, X. J. Wang, S. H. Glenzer, Heterogeneous to homogeneous melting transition visualized with ultrafast electron diffraction. *Science* **360**, 1451–1455 (2018).
15. P. Emma, R. Akre, J. Arthur, R. Bionta, C. Bostedt, J. Bozek, A. Brachmann, P. Bucksbaum, R. Coffee, F.-J. Decker, Y. Ding, D. Dowell, S. Edstrom, A. Fisher, J. Frisch, S. Gilevich, J. Hastings, G. Hays, P. Hering, Z. Huang, R. Iverson, H. Loos, M. Messerschmidt, A. Miahnahri, S. Moeller, H.-D. Nuhn, G. Pile, D. Ratner, J. Rzepiela, D. Schultz, T. Smith, P. Stefan, H. Tompkins, J. Turner, J. Welch, W. White, J. Wu, G. Yocky, J. Galayda, First lasing and operation of an ångstrom-wavelength free-electron laser. *Nat. Photonics* **4**, 641–647 (2010).
16. L. B. Fletcher, H. J. Lee, T. Döppner, E. Galtier, B. Nagler, P. Heimann, C. Fortmann, S. LePape, T. Ma, M. Millot, A. Pak, D. Turnbull, D. A. Chapman, D. O. Gericke, J. Vorberger, T. White, G. Gregori, M. Wei, B. Barbrel, R. W. Falcone, C.-C. Kao, H. Nuhn, J. Welch, U. Zastrau, P. Neumayer, J. B. Hastings, S. H. Glenzer, Ultrabright X-ray laser scattering for dynamic warm dense matter physics. *Nat. Photonics* **9**, 274–279 (2015).
17. T. Kluge, M. Rödel, J. Metzkes, A. Pelka, A. L. Garcia, I. Prencipe, M. Rehwald, M. Nakatsutsumi, E. E. McBride, T. Schönherr, M. Garten, N. J. Hartley, M. Zacharias, A. Erbe, Y. M. Georgiev, E. Galtier, I. Nam, H. J. Lee, S. Glenzer, M. Bussmann, C. Gutt, K. Zeil, C. Rödel, U. Hübner, U. Schramm, T. E. Cowan, Observation of ultrafast solid-density plasma dynamics using femtosecond X-ray pulses from a free-electron laser. *Phys. Rev. X* **8**, 031068 (2018).
18. B. J. Siwick, J. R. Dwyer, R. E. Jordan, R. J. D. Miller, Femtosecond electron diffraction studies of strongly driven structural phase transitions. *Chem. Phys.* **299**, 285–305 (2004).
19. F. Seiboth, L. B. Fletcher, D. McGonegle, S. Anzellini, L. E. Dresselhaus-Cooper, M. Frost, E. Galtier, S. Goede, M. Harmand, H. J. Lee, A. L. Levitan, K. Miyanishi, B. Nagler, I. Nam, N. Ozaki, M. Rödel, A. Schropp, C. Spindloe, P. Sun, J. S. Wark, J. Hastings, S. H. Glenzer, E. E. McBride, Simultaneous 8.2 keV phase-contrast imaging and 24.6 keV X-ray diffraction from shock-compressed matter at the LCLS. *Appl. Phys. Lett.* **112**, 221907 (2018).
20. X. J. Wang, D. Xiang, T. K. Kim, H. Ihee, Potential of femtosecond electron diffraction using near-relativistic electrons from a photocathode RF electron gun. *J. Korean Phys. Soc.* **48**, 390–396 (2006).
21. R. Li, C. Tang, Y. Du, W. Huang, Q. Du, J. Shi, L. Yan, X. Wang, Experimental demonstration of high quality MeV ultrafast electron diffraction. *Rev. Sci. Instrum.* **80**, 083303 (2009).
22. I. Cook, Materials research for fusion energy. *Nat. Mater.* **5**, 77–80 (2006).
23. K. Nordlund, C. Björkas, T. Ahlgren, A. Lasa, A. E. Sand, Multiscale modelling of plasma–wall interactions in fusion reactor conditions. *J. Phys. D: Appl. Phys.* **47**, 224018 (2014).
24. J. Knaster, A. Moeslang, T. Muroga, Materials research for fusion energy. *Nat. Phys.* **12**, 424–434 (2016).
25. A. E. Sand, S. L. Dudarev, K. Nordlund, High-energy collision cascades in tungsten: Dislocation loops structure and clustering scaling laws. *EPL* **103**, 46003 (2013).
26. P. Sun, Y. Wang, M. Frost, C. Schönwälder, A. L. Levitan, M. Mo, Z. Chen, J. B. Hastings, G. R. Tynan, S. H. Glenzer, P. Heimann, Characterization of defect clusters in ion-irradiated tungsten by X-ray diffuse scattering. *J. Nucl. Mater.* **510**, 322–330 (2018).
27. Z. Lin, L. V. Zhigilei, Time-resolved diffraction profiles and atomic dynamics in short-pulse laser-induced structural transformations: Molecular dynamics study. *Phys. Rev. B* **73**, 184113 (2006).
28. X. D. Dai, Y. Kong, J. H. Li, B. X. Liu, Extended Finnis-Sinclair potential for bcc and fcc metals and alloys. *J. Phys.: Condens. Matter* **18**, 4527–4542 (2006).
29. I. T. Todorov, W. Smith, K. Trachenko, M. T. Dove, DL_POLY_3: New dimensions in molecular dynamics simulations *via* massive parallelism. *J. Mater. Chem.* **16**, 1911–1918 (2006).
30. Z. Lin, E. Leveugle, E. M. Bringa, L. V. Zhigilei, Molecular dynamics simulation of laser melting of nanocrystalline Au. *J. Phys. Chem. C* **114**, 5686–5699 (2010).
31. D. R. Lide, *CRC Handbook of Chemistry and Physics* (CRC Press, ed. 97, 2017).
32. A. R. Miedema, F. J. den Broeder, On the interfacial energy in solid-liquid and solid-solid metal combinations. *Z. Metallkd.* **70**, 14 (1979).
33. M. Z. Mo, X. Shen, Z. Chen, R. K. Li, M. Dunning, K. Sokolowski-Tinten, Q. Zheng, S. P. Weathersby, A. H. Reid, R. Coffee, I. Makasyuk, S. Edstrom, D. McCormick, K. Jobe, C. Hast, S. H. Glenzer, X. Wang, Single-shot mega-electronvolt ultrafast electron diffraction for structure dynamic studies of warm dense matter. *Rev. Sci. Instrum.* **87**, 11D810 (2016).
34. S. P. Weathersby, G. Brown, M. Centurion, T. F. Chase, R. Coffee, J. Corbett, J. P. Eichner, J. C. Frisch, A. R. Fry, M. Gühr, N. Hartmann, C. Hast, R. Hettel, R. K. Jobe, E. N. Jongewaard, J. R. Lewandowski, R. K. Li, A. M. Lindenberg, I. Makasyuk, J. E. May, D. McCormick, M. N. Nguyen, A. H. Reid, X. Shen, K. Sokolowski-Tinten, T. Vecchione, S. L. Vetter, J. Wu, J. Yang, H. A. Dürr, X. J. Wang, Mega-electron-volt ultrafast electron diffraction at SLAC National Accelerator Laboratory. *Rev. Sci. Instrum.* **86**, 073702 (2015).
35. www.norcada.com.
36. www.srim.org/SRIM/SRIMLEGL.htm.
37. M. H. J. 't Hoen, M. Mayer, A. W. Kleyn, P. A. Zeijlmans van Emmichoven, Strongly reduced penetration of atomic deuterium in radiation-damaged tungsten. *Phys. Rev. Lett.* **111**, 225001 (2013).
38. T. L. Bergman, A. S. Lavine, F. P. Incropera, D. P. Dewitt, *Fundamentals of Heat and Mass Transfer* (John and Wiley, ed. 7, 2011).
39. Z. Lin, L. V. Zhigilei, V. Celli, Electron-phonon coupling and electron heat capacity of metals under conditions of strong electron-phonon nonequilibrium. *Phys. Rev. B* **77**, 075133 (2008).

40. D. M. Duffy, A. M. Rutherford, Including the effects of electronic stopping and electron-ion interactions in radiation damage simulations. *J. Phys. Condens. Matter* **19**, 016207 (2007).
41. S. L. Daraszewicz, Y. Giret, H. Tanimura, D. M. Duffy, A. L. Shluger, K. Tanimura, Determination of the electron-phonon coupling constant in tungsten. *Appl. Phys. Lett.* **105**, 023112 (2014).
42. W. Steinhögl, G. Steinlesberger, M. Perrin, G. Scheinbacher, G. Schindler, M. Traving, M. Engelhardt, Tungsten interconnects in the nano-scale regime. *Microelectron. Eng.* **82**, 266–272 (2005).
43. C. Y. Ho, R. W. Powell, P. E. Liley, Thermal conductivity of the elements: A comprehensive review. *J. Phys. Chem. Ref. Data* **3**, 1–10 (1974).
44. F. C. Nix, D. MacNair, The thermal expansion of pure metals: Copper, gold, aluminum, nickel, and iron. *Phys. Rev.* **60**, 597–605 (1941).
45. L.-M. Peng, S. Dudarev, M. J. Whelan, *High Energy Electron Diffraction and Microscopy* (Oxford Univ. Press, 2004).
46. E. Lorch, Neutron diffraction by germania, silica and radiation-damaged silica glasses. *J. Phys. C: Solid State Phys.* **2**, 229–237 (1969).
47. K. Laaziri, S. Kycia, S. Roorda, M. Chicoine, J. L. Robertson, J. Wang, S. C. Moss, High-energy X-ray diffraction study of pure amorphous silicon. *Phys. Rev. B* **60**, 13520–13533 (1999).

Acknowledgments: We thank SLAC management for the strong support. We acknowledge the technical support of SLAC Accelerator Directorate, Technology Innovation Directorate, LCLS Laser Science and Technology Division, and Test Facilities Department. We also thank the technical support on ion irradiation experiments from the Center for Integrated Nanotechnologies, a DOE nanoscience user facility jointly operated by Los Alamos and Sandia National Laboratories. **Funding:** This work was supported by the DOE Fusion Energy Sciences under FWP no. 100182 and the U.S. Department of Energy contract no. DE-AC02-76SF00515 and partially supported by the DOE BES Accelerator and Detector R&D program and the SLAC UED/UEM Initiative Program Development Fund. S.M. acknowledges funding from EPSRC under the grant codes EP/R006288/1 and EP/R0029431. **Author contributions:** S.G. and M.M. conceived the study. M.M., Z.C., R.L., Y.W., and X.W. performed the experiments. M.M. analyzed the UED data. M.M., Z.C., S.M., and S.G. interpreted the data. S.M. and P.F. performed and analyzed the MD simulations. M.M., S.M., and S.G. wrote the manuscript with input from all authors. **Competing interests:** The authors declare that they have no competing interests. **Data and materials availability:** All data needed to evaluate the conclusions in the paper are present in the paper and/or the Supplementary Materials. The datasets generated and analyzed during this study are available from the corresponding authors upon reasonable request.

Submitted 12 November 2018
Accepted 12 April 2019
Published 24 May 2019
10.1126/sciadv.aaw0392

Citation: M. Mo, S. Murphy, Z. Chen, P. Fossati, R. Li, Y. Wang, X. Wang, S. Glenzer, Visualization of ultrafast melting initiated from radiation-driven defects in solids. *Sci. Adv.* **5**, eaaw0392 (2019).